Chaotic, subduction-like downflows in a spherical model of convection in the Earth's mantle

Gary A. Glatzmaier*, Gerald Schubert† & Dave Bercovici‡

* Earth and Environmental Sciences Division and
Institute of Geophysics and Planetary Physics,,
Los Alamos National Laboratory, Los Alamos, New Mexico 87545, USA
† Department of Earth and Space Sciences and
Institute of Geophysics and Planetary Physics, University of California,
Los Angeles, California 90024, USA
‡ Department of Geology and Geophysics,
Woods Hole Oceanographic Institution, Woods Hole,
Massachusetts 02543, USA

NUMERICAL models of three-dimensional, nonlinear, thermal convection of very viscous fluids have recently been developed in rectangular[1–4] and spherical[5–12] geometries as analogues of convection in the Earth's mantle. Here we describe model calculations for a compressible fluid in a three-dimensional spherical shell with 80% of the surface heat flow generated within the model mantle, in agreement with estimates for the Earth's mantle[13]. The Rayleigh number and the numerical resolution for these calculations are greater than those of our previous studies[9,10] of internally heated convection in a spherical shell. Our numerical solutions are strongly chaotic, with surface planforms dominated by long curvilinear downflows reminiscent of the descending slabs in the Earth's mantle. Although analogy to the Earth's mantle is necessarily imperfect, owing to, for example, the absence of variable viscosity and rheology—and hence of lithospheric plates—our results suggest that descending slabs play an important part in driving mantle convection, and that their chaotic evolution may influence the spatial and temporal behaviour of plates and thus the dispersal and aggregation of continents.

The numerical model[7] solves the nonlinear equations of motion that describe thermal convection of a newtonian (linear viscosity), infinite Prandtl number (highly viscous), anelastic compressible (no sound waves) fluid in a three-dimensional spherical shell for conditions that approximate the Earth's mantle. The thermodynamic variables and the three components of velocity are expanded in spherical harmonics (up to degree and order 85) to resolve their horizontal structures and in Chebyshev polynomials (up to degree 30) to resolve their radial structures. The nonlinear advection and viscous heating terms are calculated each timestep in grid space on 256 Fourier longitudinal levels, 128 Legendre colatitudinal levels and 33 Chebyshev radial levels. Our numerical solution is adequately resolved because the kinetic and thermal energies drop several orders of magnitude as functions of the horizontal and radial wave numbers and because the solution is in good agreement with a solution at a lower numerical resolution (spherical harmonic degree and order up to 63).

Our model lacks several important features required of fully realistic numerical simulations of mantle convection in the Earth. One is a viscosity that depends on temperature, pressure and the state of stress. Another is a variable rheology simulating the behaviour of tectonic plates. Phase and chemical transitions in the mantle also need to be modelled. Although these features will certainly affect the spatial and temporal details of the convection, we first need to learn what our present model reveals about the basic properties of time-dependent three-dimensional compressible convection in a spherical shell.

We examine a case that is partly heated within the model mantle (10^{-14} W kg^{-1}) and partly heated from the underlying core. An adiabatic polytrope with an index of 0.4 and a Grüneisen parameter of 1.1 determines the profiles of the reference-state pressure, density and temperature that approximate the Earth's mantle and about which the thermodynamic variables are perturbed. Impermeable stress-free boundary conditions are imposed on the velocity. The model temperatures are set to 3,270 K at the inner (core/mantle) boundary and 1,070 K at the outer boundary. Of the total temperature drop across the model mantle, 1,200 K is due to adiabatic compression and the rest, 1,000 K, is the superadiabatic temperature drop, which drives the convection. We specify a constant dynamic viscosity of 5.6×10^{22} kg m^{-1} s^{-1} and a constant thermal conductivity of 23 W m^{-1} K^{-1}. Owing to computing limitations, the thermal conductivity adopted in the model is about five times larger than the conductivity of actual mantle rocks. The volume-averaged Rayleigh number Ra (a measure of the convective vigour[7]) due to both the superadiabatic temperature drop and the internal heating is 1.6×10^{6}. This is ~200 times greater than the critical Rayleigh number required for the onset of convection, but probably still ~10 times smaller than the average value for the Earth's mantle. We use a timestep of 10^{6} years, one quarter of the Courant condition, and start from small random initial perturbations in the entropy (temperature) field[7].

The resulting time-averaged heat flows through the inner and outer boundaries are 1×10^{13} W and 5×10^{13} W, respectively. Thus, ~80% of the heat conducted through the outer boundary is generated in the model mantle. The total heat flow through the outer boundary is comparable to the heat flow through the Earth's surface. In the bulk of the model mantle >90% of the heat flow is convective and <10% is conductive. Maximum convective velocities in the model are ~30 mm yr^{-1}, comparable to the observed velocities of tectonic plates.

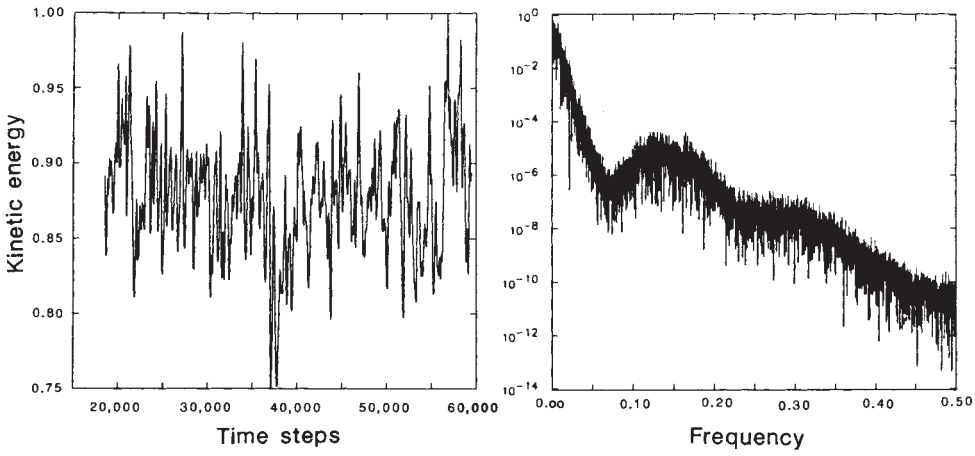

FIG. 1 Total kinetic energy as a function of the timestep and its power spectrum as a function of frequency (in cycles per second scaled by the timestep). Both plots are normalized to unity. For this long-time integration we truncated the spherical harmonic expansions at $l=63$ instead of 85.

The total kinetic energy in the model mantle is plotted in Fig. 1 as a function of time for the last 40,000 timesteps of the calculation. The large amplitude variation illustrates the time dependence of the solution; however, the basic qualitative features of the convection do not change over this period of time. Also plotted in Fig. 1 is the square of the Fourier transform of the kinetic energy time series as a function of frequency. The broadband distribution of power is indicative of a chaotic system. In addition, the phase space representation of kinetic energy as a function of its time rate of change (not displayed here) shows no limit cycle or torus, indicating chaos. Two popular methods for calculating the fractal dimension[14,15] failed to converge, suggesting a high fractal dimension for our three-dimensional convection. Our results support the conclusion, made on the basis of two-dimensional calculations[16-18], that mantle convection in the Earth is chaotic. Our results suggest, however, that mantle convection is much more chaotic than the low-fractal-dimension solutions obtained with the two-dimensional models using low Rayleigh numbers and no internal or viscous heating.

A typical snapshot of the spatial patterns of the temperature and velocity fields on three different surfaces of constant radius is shown in Fig. 2. In the upper part of the sphere, cold dense fluid tends to converge and sink in long narrow sheets surrounded by a weak background of warm buoyant diverging upflow. This thin sheet-like downflow, initiated by the thin thermal boundary layer at the top, tends to break up with increasing depth into cylindical downflow plumes that squeeze the hot fluid between them as they impinge on the inner boundary forcing hot cylindrical upflow plumes at the vertices of the connected network of warm fluid. These upflow plumes expand in the upper part of the sphere forming the weak background of upwelling there.

The formation of the upwelling plumes at the intersections of warm linear thermals is similar to the spoke pattern of convection observed in laboratory and numerical studies of plane-layer convection with constant viscosity and all heating from the bottom of the fluid layer[2,4,19]. Purely bottom-heated convection in spherical shells does not result in such spoke patterns and in fact maintains upwelling plumes surrounded by downwelling sheets over the entire depth of the shell; the contrast with plane-layer convection is primarily because of the breaking of the mid-plane symmetry by the spherical geometry[7,9,20]. Thus, the similarity of our internally heated solutions to bottom-heated plane-layer convection implies that the mid-plane symmetry is partially restored by internal heating in the spherical shell (by equalizing the temperature drops across the top and bottom boundary layers, for example). Unlike plane-layer convection, however, the network of linear thermals is more prominent in the temperature field (which is what the shadowgraphs in laboratory experiments detect), whereas the strong upwelling motion is primarily confined to cylindrical plumes.

Three snapshots, 200 million years apart, of the spatial patterns of the temperature and velocity fields in a typical cross-

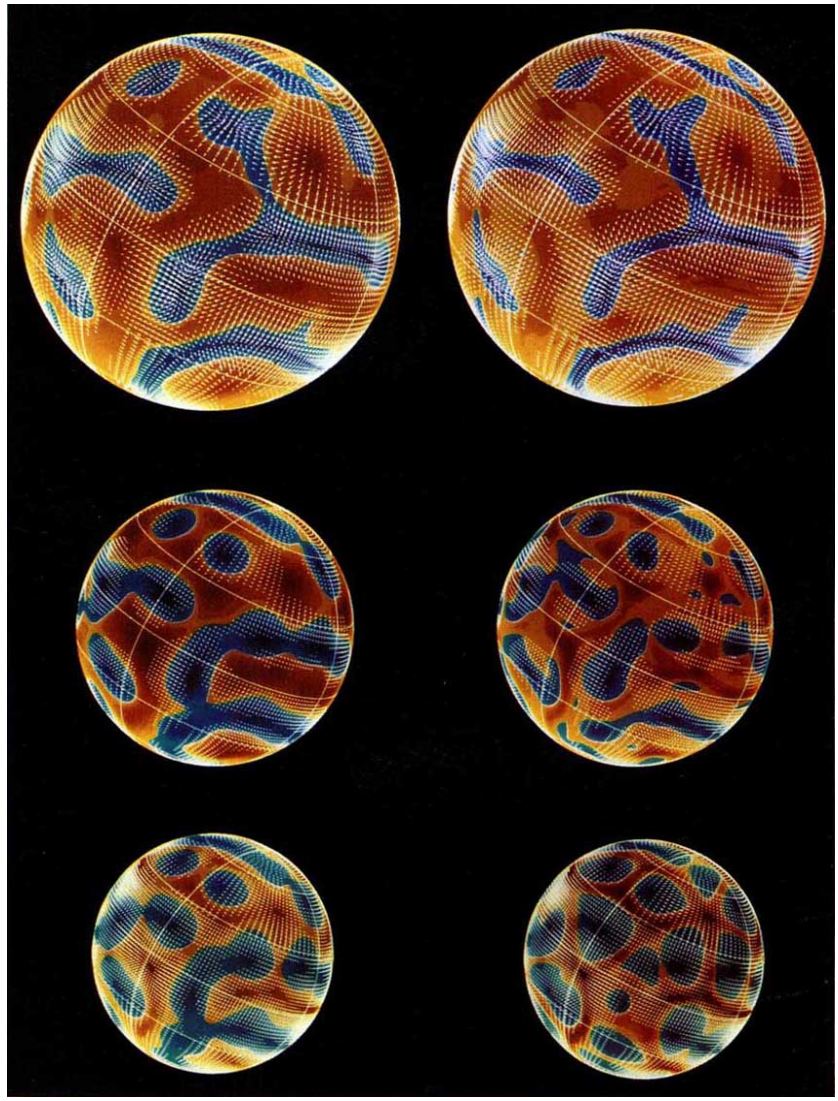

FIG. 2 Plots (all at the same timestep) of convective velocities and temperatures in three different constant-radius surfaces (5,940, 4,350 and 3,770 km). These spherical surfaces are scaled according to their radii. The colours in the three plots on the left represent the radial component of velocity with a contour increment of 1.5 mm yr^{-1}. Reds and yellows represent upflow (a maximum of 12.0 mm yr^{-1}); blues represent downflow (a maximum of 19.5 mm yr^{-1}). The colours in the three plots on the right represent the temperature relative to the spherically averaged value at each radius with a contour increment of 50 K. Reds and yellows represent hot fluid (a maximum of +400 K); blues represent cold fluid (a minimum of −650 K). The arrows represent the direction and amplitude of the horizontal velocity in these surfaces. All are scaled in the same way, with a maximum of 20 mm yr^{-1}. Velocities less than 2 mm yr^{-1} are not plotted.

sectional slice through the spherical shell are illustrated in Fig. 3. A typical cold boundary layer instability at '12 o'clock' is developing in the first (top) plot. It has sunk to mid-depth in the second (middle) plot, and is spreading along the lower boundary in the third (bottom) plot. Figures 2 and 3 show how the spatial scale of the temperature is smaller than that of the velocity (owing to the small thermal diffusivity compared to kinematic viscosity) and how at certain times and places relatively hot fluid is dragged downward.

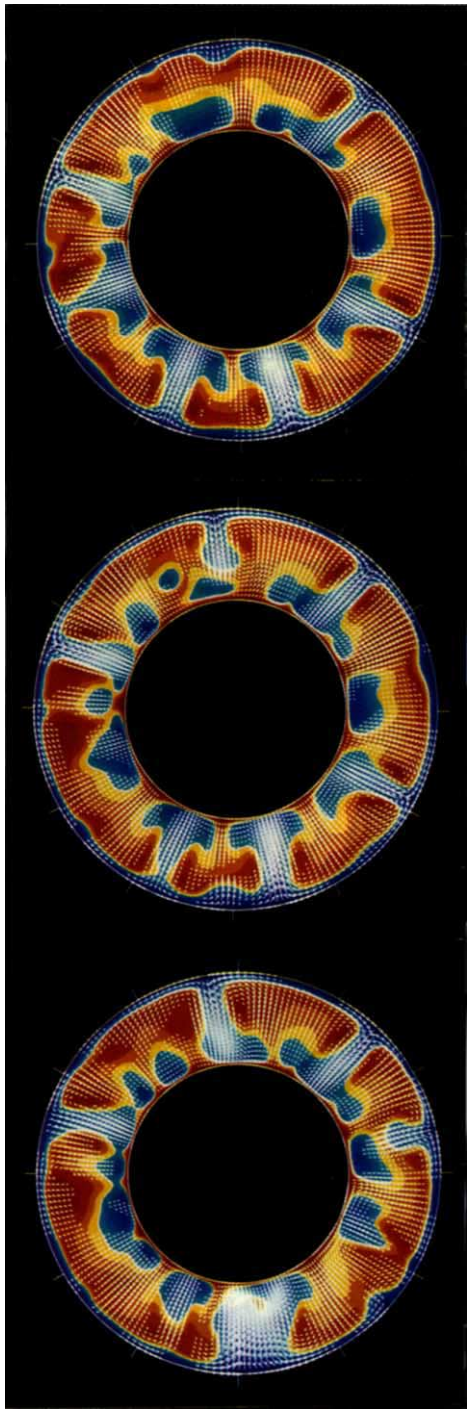

FIG. 3 Plots (in the same cross-sectional slice through the three-dimensional shell) of convective velocities and temperatures at three different times separated by 200 timesteps (200 million years) beginning with the top plot. The colours represent the temperature relative to the radially dependent adiabatic temperature profile with a contour increment of 50 K. Reds and yellows represent hot fluid (a maximum of 300 K); blues represent cold fluid (a minimum of −750 K). The arrows represent the velocities in this cross-sectional surface and are scaled the same way as those in Fig. 2.

A movie of this numerical simulation shows the convection pattern continuously changing, with the hot upflow passively reacting to the dominant cold downflow. The long downflow sheets in the upper part of the sphere sometimes contract or break up, forming cylindrical-like downwelling features and at other times the downflow sheets link up forming even longer sheet-like features. Downwellings form spontaneously over regions that are warm at depth. Although the convection pattern is very chaotic, the basic spatial and temporal characteristics of the convection do not change after the decay of the initial transients.

We can compare these results to our previous calculations with 50% and 80% internal heating[9,10] which were run at lower Rayleigh numbers and at a resolution a factor of two lower in both latitude and longitude. Although the previous patterns were time-dependent, the present results are more temporally complex and definitely chaotic. In our earlier calculations convection patterns tended to be anchored to the upwelling plumes which were relatively steady in number and location. In contrast, the upwelling plumes in our present calculations are more variable in number and location owing to their interaction with chaotic downwelling. At even higher Rayleigh numbers than in the present calculation (stronger thermal driving relative to viscous and thermal diffusion), convection will probably have greater spatial and temporal structure and modelling will require still better numerical resolution. Higher numerical resolution (and therefore more computing resources) will also be required when three-dimensional models account for variable viscosity, tectonic plates and phase and chemical transitions. It is difficult to predict how these needed improvements will alter the structure of the simulated convection. It is, however, encouraging that the sheet-like downwellings seen in our previous calculations at 80% internal heating[10] also dominate the structure of convection here. This qualitative agreement gives us confidence that this downwelling pattern will continue to be an important feature as models of mantle convection become more realistic.

If the numerical model presented here is sufficiently representative of the Earth's mantle, the numerical results have significant implications for the nature of mantle convection. Convection in the model is predominantly controlled by the largely sheet-like downwellings, suggesting that the descending slabs in the Earth are the main drive for plate motions and mantle convection[21]. The prominent role of downwellings in convecting systems heated strongly from within has also been demonstrated in other numerical studies[2,4,8–10] and in laboratory experiments[22,23]. The lengthening of downwellings in the model along their axes suggests the possibility that subduction zones on Earth may evolve by propagation along their strike[4]. In our model, the downwelling sheets also drift perpendicular to their axes, similar to the lateral migration (perpendicular to strike) of descending slabs through the mantle[24]. Because subducting slabs probably drive plate tectonics, their chaotic migration and propagation (inferred from these numerical calculations) may also have a role in the apparently random dispersal and aggregation of continents.

As the upflow in our calculations takes the form of cylindrical plumes, our results support the evidence that mid-ocean ridges are the result of passive rifting[9,25]. The upwelling plumes in our model broaden with height. A temperature-dependent viscosity would probably focus the thermal and velocity anomalies of plumes into smaller-diameter cylindrical structures and flatten the heads of plumes more dramatically as they encounter the base of the strong lithosphere[26,27]. These plumes probably weaken the lithosphere and determine where the lithosphere tears and spreads apart in response to slab pull. This may be one reason why many hot spots are preferentially located near mid-ocean ridges[28]. □

Received 15 May; accepted 1 August 1990.

1. Cserepes, L., Rabinowics, M. & Romberg-Borot, C. *J. geophys. Res.* **93,** 12009–12025 (1988).
2. Houseman, G. *Nature* **332,** 346–349 (1988).
3. Travis, B., Olson, P. & Schubert, G. *J. Fluid Mech.* **216,** 71–91 (1990).
4. Travis, B., Weinstein, S. & Olson, P. *Geophys. Res. Lett.* **17,** 243–246 (1990).
5. Baumgardner, J. R. *J. statist Phys.* **39,** 501–511 (1985).
6. Machetel, P., Rabinowicz, M. & Bernardet, P. *Geophys. astrophys. Fluid Dyn.* **37,** 57–84 (1986).
7. Glatzmaier, G. A. *Geophys. astrophys. Fluid Dyn.* **43,** 223–264 (1988).
8. Baumgardner, J. R. in *Physics of the Planets* (ed. Runcorn, S. K.) 199–231 (Wiley, New York, 1988).
9. Bercovici, D., Schubert, G & Glatzmaier, G. A. *Science* **244,** 950–955 (1989).
10. Bercovici, D., Schubert, G & Glatzmaier, G. A. *Geophys. Res. Lett.* **16,** 617–620 (1989).
11. Bercovici, D., Schubert, G., Glatzmaier, G. A. & Zebib, A. *J. Fluid Mech.* **206,** 75–104 (1989).
12. Schubert, G., Bercovici, D. & Glatzmaier, G. A. *J. geophys, Res.* (in the press).
13. Turcotte, D. L. & Schubert, G. *Geodynamics* (Wiley, New York, 1982).
14. Grassberger, P. & Procaccia, I. *Phys. Rev. Lett.* **50,** 346–349 (1983).
15. Kostelich, E. J. & Swinney, H. L. *Physica Scripta* **40,** 436–441 (1989).
16. Machetel, P. & Yuen, D. A. *Earth planet Sci. Lett.* **86,** 93–104 (1987).
17. Vincent, A. P. & Yuen, D. A. *Phys. Rev.* **A38,** 328–334 (1988).
18. Stewart, C. A. & Turcotte, D. L. *J. geophys. Res.* **94,** 13707–13717 (1989).
19. Whitehead, J. A. & Parsons, B. *Geophys. astrophys. Fluid Dyn.* **9,** 201–217 (1978).
20. Busse, F. H. *J. Fluid Mech.* **72,** 67–85 (1975).
21. Schubert, G. in *Mechanisms of Continental Drift and Plate Tectonics* (eds Davies, P. A. & Runcorn, S. K.) 151–158 (Academic, London, 1980).
22. Carrigan, C. R. *Geophys. astrophys. Fluid Dyn.* **32,** 1–21 (1985).
23. Weinstein, S. A. & Olson, P. *Geophys. Res. Lett.* **17,** 239–242 (1990).
24. Garfunkel, Z. & Schubert, G. *J. geophys. Res.* **91,** 7205–7223 (1986).
25. Lachenbruch, A. H. *J. geophys. Res.* **81,** 1883–1902 (1976).
26. Olson, P., Schubert, G., Anderson, C. & Goldman, P. J. *J. geophys, Res.* **93,** 15065–15084 (1988).
27. Schubert, G., Olson, P., Anderson, C. & Goldman, P. *J. geophys. Res.* **94,** 9523–9532 (1989).
28. Weinstein, S. A. & Olson, P. *Geophys Res. Lett.* **16,** 433–436 (1989).

ACKNOWLEDGEMENTS. We thank the participants of the Los Alamos Mantle Convection Workshop for discussions, and acknowledge support from the Institute of Geophysics and Planetary Physics at the Los Alamos National Laboratory, the NASA Geodynamics Program, and the Center for Earth and Planetary Interiors, UCLA. We also thank D. Langley for developing the graphics software.

Enhancement of nitrogen deposition to forest trees exposed to SO_2

A. R. McLeod*, M. R. Holland†, P. J. A. Shaw*, P. M. Sutherland*, N. M. Darrall* & R. A. Skeffington*

* Terrestrial Ecology Group, National Power Technology and Environmental Centre, Kelvin Avenue, Leatherhead, Surrey KT22 7SE, UK
† Department of Biology, Imperial College, Silwood Park, Ascot, Berkshire SL5 7PY, UK

DEPOSITION of atmospheric nitrogen compounds, particularly ammonia, is postulated to have a variety of deleterious effects[1], including damage to soils, trees and other vegetation[1–6]. We report here that fumigation of coniferous trees in the open air with sulphur dioxide (13 and 22 p.p.b.–parts in 10^9 by volume) produced an increased deposition of atmospheric NH_3 to foliage. A mechanism for co-deposition of NH_3 and SO_2 to wet surfaces has been suggested[7,8]. As concentrations of NH_3 at the site are not unusually high (annual mean, 4 p.p.b.)[9], this mechanism may enhance nitrogen deposition over large areas of Europe. It may also account for some results of experimental fumigations previously attributed to SO_2 alone.

The experimental site is located at Liphook, Hampshire, UK and uses a technique previously developed to fumigate cereals with SO_2 (ref. 10). In 1985 seven plots (Fig. 1) were planted with seedlings of Scots pine (*Pinus sylvestris*), Sitka spruce (*Picea sitchensis*) and Norway spruce (*Picea abies*)[11]. Concentrations for SO_2 treatments were multiples (1.5 and 3 times) of sequential hourly mean concentrations measured in 1979–1980 at a rural site in central England[12]. Target values for ozone treatments were a constant multiple (1.5 times) of the measured ambient O_3 at the site. Including ambient concentrations, this gives a 2×3 factorial design with one additional ambient plot (Fig. 1). Exposure to SO_2 commenced in May 1987 and O_3 fumigation occurred from March–December 1988 and May–December 1989.

Each October, eight trees of each species per plot were harvested for biometric and chemical analysis. The foliar content of nitrogen, sulphur and cations was determined by standard methods[13]. In summer 1989, throughfall collectors (diameter, 0.9 m) were fitted to four trees each of Scots pine and Sitka spruce in plots 2–7. Samples were collected fortnightly and analysed separately.

In October 1988 the foliar nitrogen content of Norway spruce showed a clear trend with SO_2 treatment, being 1.7 times higher in the high-SO_2 plots than in the ambient plots (Fig. 2). Sulphur content of the needles also reflected the SO_2 treatments (Fig. 2). A similar trend in foliar nitrogen was observed in Sitka spruce, but not in Scots pine. Needles of Norway spruce on plots without SO_2 fumigation were below the deficiency level of 12 mg N g^{-1} in October 1988 (Fig. 2); needles of Sitka spruce on all plots were likewise deficient, whereas those of Scots pine remained above the deficiency level of 11 mg N g^{-1} (ref. 14). Estimates of the total nitrogen content of needle biomass in October 1988 revealed that the Norway spruce and Sitka spruce contained more nitrogen (7.8 kg ha^{-1} and 12.8 kg ha^{-1}, respectively) in the 22 p.p.b. SO_2 plots than trees in ambient plots.

There are several mechanisms that might explain this difference in nitrogen, including N_2 fixation, litter decomposition, reallocation from roots, changes in understorey vegetation and atmospheric inputs. Studies of the soil nitrogen cycle[15] found no evidence for differences in N_2 fixation or nitrogen mineralization. It is possible that SO_2 effects have suppressed the nitrogen demand of understorey vegetation, but there is no evidence for this. Likewise, studies of below-ground biomass have shown no indication of treatment effects (although with large errors), and reallocation of nitrogen from needles prematurely lost in SO_2-treated plots would not supply enough nitrogen to explain the effect. The most probable explanation for the increased nitrogen appears to be a known mechanism for SO_2 enhancement of NH_3 deposition to wet surfaces[7,8]. The solubility of SO_2 or NH_3 alone is limited by the pH of the acidic or basic solution they form, respectively, whereas with both gases together, the pH can remain at non-limiting values, so enhancing solubility and deposition. Evidence to support this comes from measurements of ammonium ion in throughfall and measured deposition to water surfaces within the plots.

Ammonium in throughfall has been measured from July 1989

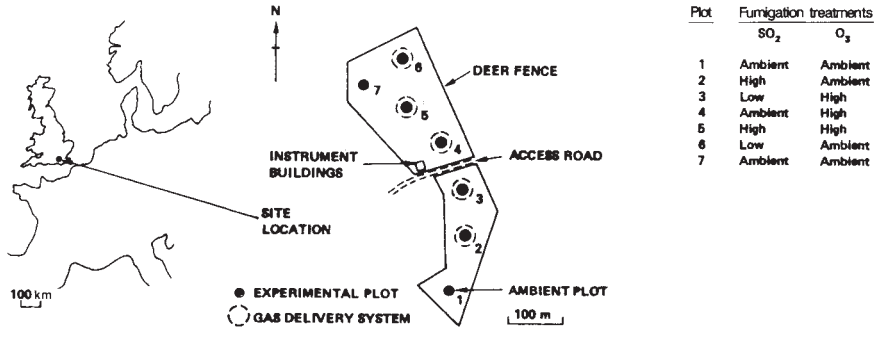

FIG. 1 Map of Europe showing the location of the study site, the layout of the experimental plots and gaseous treatments. The plots were planted with 196 seedlings of each species at 1-m spacing in a 25-m diameter area within a 50-m diameter circle of gas sources[11].